

## Battery state-of-health estimation using CNNs with transfer learning and multi-modal fusion of partial voltage profiles and histogram data

Junran Chen <sup>a,\*</sup> , Phillip Kollmeyer <sup>a</sup> , Ryan Ahmed <sup>b</sup> , Ali Emadi <sup>a, b</sup>

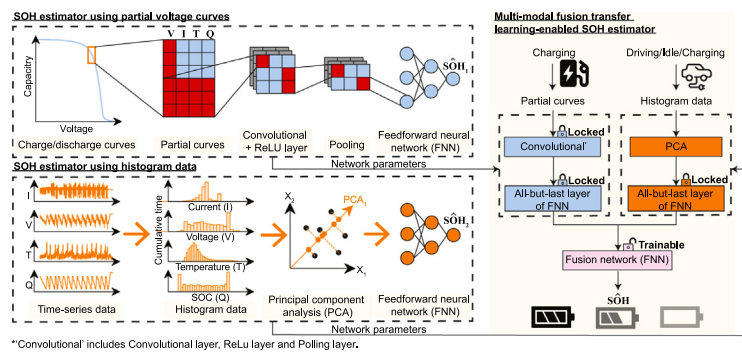
<sup>a</sup> Department of Electrical & Computer Engineering, McMaster University, 1280 Main St W, Hamilton, L8S 4L7, Ontario, Canada

<sup>b</sup> Department of Mechanical Engineering, McMaster University, 1280 Main St W, Hamilton, L8S 4L7, Ontario, Canada

### HIGHLIGHTS

- Partial voltage curves can lead to misleading diagnoses of battery health.
- Histogram data require extensive training sets to capture battery health.
- The proposed multi-modal fusion model diagnoses battery health from varying sources.
- Using partial voltage curves and histogram data with multi-modal fusion significantly enhances the accuracy and feasibility of battery health diagnostics.

### GRAPHICAL ABSTRACT



### ARTICLE INFO

#### Keywords:

Convolutional neural network  
Lithium-ion battery  
Multi-modal fusion  
State of health estimation  
Transfer learning

### ABSTRACT

Accurate estimation of battery state of health (SOH) is critical for ensuring safe and reliable operation, enabling health-conscious control, and supporting second-life applications. Existing health indicators (HIs) used in data-driven models have practicality, accuracy, and robustness limitations. For instance, partial voltage or incremental capacity curves may lead to misleading SOH estimations, while histogram-based methods require extensive training data. This paper proposes a multi-modal fusion model that integrates two types of HIs extracted from partial voltage curves recorded during charging and histogram data during operation. By addressing the limitations of both types of HIs, the proposed model achieves superior performance in terms of accuracy and robustness. The proposed model is validated on two representative datasets, achieving a root mean squared percentage error (RMSPE) as low as 0.74 %, reducing estimation error by up to 42 % compared to existing models and requiring 60 % less training data. The results demonstrate the feasibility and advantages of combining HIs from different sources, underscoring the importance of detailed feature analysis in developing data-driven models for battery state estimation.

### 1. Introduction

Lithium-ion batteries are widely recognized as efficient energy storage devices for applications ranging from small electrical devices (e.g.

cell phones and laptops) to heavy-duty systems like electric vehicles (EVs), thanks to their outstanding features of high energy density, low self-discharge rate and wide operating temperature range [1]. However, due to undesired side reactions occurring inside the cell, such as lithium

\* Corresponding author.

Email address: [chenj425@mcmaster.ca](mailto:chenj425@mcmaster.ca) (J. Chen).

Nomenclature	
CC	Constant current
CCCV	Constant current constant voltage
CNN	Convolutional neural network
CV	Constant voltage
DTW	Dynamic time warping
EV	Electric vehicle
FNN	Feedforward neural network
GPR	Gaussian process regression
HIs	Health indicators
HPPC	Hybrid pulse power characterization
HWFET	Highway fuel economy test
IC	Incremental capacity
ICA	Incremental capacity analysis
LA92	Unified cycle driving test
LFP	Lithium iron phosphate
LSTM	Long short-term memory network
MAPE	Mean absolute percentage error
NCA	Lithium nickel cobalt aluminum oxides
PCA	Principal component analysis
RFR	Random forest regression
RMSPE	Root mean squared percentage error
SEI	Solid electrolyte interphase
SOC	State of charge
SOH	State of health
SVM	Support vector machine
SVR	Support vector regression
UDDS	Urban dynamometer driving schedule
WLTP	Worldwide harmonized light vehicle test procedure

plating [2], solid electrolyte interphase (SEI) growth [3], and electrode material cracking [4], the battery inevitably ages over time, resulting in capacity and power fade. This significantly affects battery performance and safety, making battery health monitoring and management solutions essential [5]. A battery's state of health (SOH) is a crucial metric for monitoring its health status, referred to as the ratio between discharge capacity at a constant C-rate from a fully charged state and the rated/nominal capacity in this work. For most applications, battery end-of-life is defined when its SOH drops to 80 % or 70 % [6], after which it may be repurposed for second-life applications [7], such as grid and household energy storage systems.

Accurate SOH monitoring and aging behaviour prediction enable the realization of further applications, including timely battery pack maintenance and replacement, efficient utilization of second-life applications [7] and health-conscious operation control [8]. In second-life applications, retired batteries from electric vehicles can be repurposed for stationary energy storage in power grids or residential systems. However, assessing the capability of such batteries requires precise SOH estimation due to heterogeneous degradation patterns. Additionally, real-time SOH estimation supports adaptive charging or EV's energy management strategies that optimize cell degradation and energy usage while enhancing predictive maintenance by detecting abnormal degradation trends early.

In practice, the SOH of a battery cannot be directly obtained during real-world operation since measuring the current maximum available capacity requires discharging the battery at a fixed current rate from fully charged status to the empty state of charge (SOC). Existing SOH estimation methods are typically categorized into model-based and data-driven approaches. In model-based battery SOH estimation approaches, battery models are first employed to simulate the behaviours of cells. For example, electrochemical models [9] use partial differential equations to simulate cell physical variables, such as mass, charge kinetics, and

SEI resistance, to assess battery SOH metrics. Alternatively, equivalent circuit models [10] mimic cell SOH behaviours through the dynamics of electric components, such as resistance and capacitor. Then, various optimization algorithms and observers, such as Kalman filter [11] and particle filter [12], are applied to identify parameters that contain SOH information by minimizing the estimation error (e.g. terminal voltage) between the model and actual measurements.

Data-driven battery SOH estimation approaches do not rely on physical battery models; instead, they directly link external measurements (e.g. current, voltage and temperature) to SOH with labelled experimental data using statistical or machine learning methods [13]. Due to the obscure relationship between raw measurement data and battery SOH, various complex machine learning methods have been extensively studied and applied for battery health analysis, e.g. support vector regression (SVR) [14], random forest regression (RFR) [15], Gaussian process regression (GPR) [16], long short-term memory network (LSTM) [17], convolutional neural network (CNN) [18] and transformer [19]. However, because a typical aging data set contains at most a thousand cycles for each cell, the limited training data size often leads to overfitting. Therefore, a key challenge in data-driven SOH estimation and aging behaviour prediction is selecting health indicators (HIs) that are practical for real-world applications and informative enough for accurate SOH assessment. As shown in Table 1, numerous HIs [20] have been applied to data-driven SOH estimation, generally grouped into three categories: (a) pre-processed HIs, (b) direct-captured HIs, and (c) statistics-based HIs.

Pre-processed HIs are commonly derived from charge or discharge curves recorded at a constant current rate, including time-based, voltage-based, and incremental capacity (IC)-based. Time-based HIs [21] refer to HIs that track the time elapsed during specific stages (e.g. constant current, CC, and constant voltage, CV) of a battery's operation within a complete charging profile. For instance, Fan et al. [22]

**Table 1**  
Summary of battery health indicators used for data-driven SOH estimation methods.

Health indicators	Pre-processed	Direct-captured	Statistic-based
Definition Examples	Manually selected features CC charge time [22] Voltage slope [24,25] IC peak area [27-29] Highest temperature [23]	Time domain data Voltage curves [18,30] IC curves [31]	Cumulative cell operation data Time histogram [15,32] Ah throughput [23] Mileage driven [33]
Advantages	• Intuitive SOH insights	• Intuitive SOH insights • Feature engineering free • Risk of overfitting • Mislead SOH	• Not require specialized tests • Diverse insights • Vague correlation with SOH • Require massive dataset
Disadvantages	★ Some are impractical ★ Require feature engineering ★ Mislead SOH		

selected constant-current charging time from selected start voltage to end voltage as one of the HIs in their adversarial encoder network-based SOH estimation model. To enhance practical applicability in real-world operating scenarios and improve robustness to varying C-rate profiles, Acquarone et al. [23] developed a SOH estimator based on a linear regression model that uses HIs including constant current charging time from an initial SOC to a final voltage, normalized by the corresponding charging time for a fresh cell. The total charge or discharge time to a constant cut-off voltage will reduce because battery resistance increases and capacity fades due to degradation. Therefore, time-based HIs contain crucial information related to cell SOH, which could be attributed to different aging mechanisms, including SEI growth and lithium plating [21]. Voltage-based health indicators (HIs), such as voltage variation over equal time intervals, slope of the voltage curve, initial charge voltage, and final cut-off voltage locations, numerically capture shifts in the shape and position of the voltage curve during charging [24] or relaxation after the battery reaches full charge [25]. These shifts correlate strongly with battery impedance and capacity dynamics due to degradation. For example, Roman et al. [24] propose a machine-learning pipeline for battery SOH estimation that includes 30 HIs, of which 23 are voltage-based features extracted from constant current constant voltage (CCCV) charge profiles (e.g. mean, slope, skewness, etc.), and apply Bayesian ridge regression, deep neural networks, GPR, and RFR to achieve accurate and robust battery SOH estimation. In contrast, Zhu et al. [25] extract similar voltage-based HIs from the relaxation process after the cell reaches full charge and use transfer learning techniques together with SVM, XGBoost, and ElasticNet to estimate battery remaining capacity. In addition to extracting time-based and voltage-based HIs from voltage curves, voltage dynamics due to cell degradation can be highlighted from the differential between voltage and capacity. Incremental capacity analysis (ICA) [26] is a typical technique used extensively to generate IC-based HIs. The values of IC peak, valley, location, peak area, and peak slope are effective features for battery aging mechanism identification [27–29].

Although pre-processed HIs are prevalent in the literature on SOH estimation and aging prediction, several concerns remain. First, many pre-processed HIs are generated from full charge or discharge profiles at a constant current rate (e.g. IC peak area, CC discharge time, highest discharge temperature, etc.), requiring specialized tests conducted under controlled laboratory conditions and are impractical to obtain in real-world applications. Second, pre-processed HIs are manually designed, which may capture only a limited subset of the information available in the raw data. Furthermore, feature engineering techniques [20] are often needed to identify the most relevant HIs further, adding extra complexity and effort to the SOH estimation process.

Direct-captured HIs are automatically extracted from battery operation data using machine learning techniques, eliminating the need for complex feature engineering. To ensure the availability of direct-captured HIs in real-life usage, partial charge or discharge profiles at a constant current rate, rather than complete curves, are commonly considered. For instance, Chemali et al. [30] and Chen et al. [18] employ a CNN to directly map current, voltage, and temperature signals recorded from partial charge curves to SOH estimation. Wang et al. [34] apply a graph neural network to estimate battery remaining capacity from graph-transformed battery measurement data. Zhu et al. [31] introduce a feature fusion technique that combines information from partial voltage, IC, and  $\Delta Q$ -V curves through convolutional layers for online SOH estimation. In [35], a bilateral branched visual transformer with a dilated self-attention model captures SOH information directly from partial charge profiles. In summary, direct-captured HIs offer more insightful information than pre-processed HIs, as they are directly extracted from raw data without any loss of information due to feature engineering. However, overfitting is a significant concern for direct-captured HIs. Without a manual feature selection process, machine learning models may inadvertently learn irrelevant patterns in the data rather than the desired SOH information. Therefore, researching

methods to guide the effective training of powerful machine learning models is of great value in mitigating this issue. In addition, HIs extracted from voltage or IC curves can mismatch SOH, which will be further discussed in Section 3.1.

While both pre-processed and direct-captured HIs focus on the gradual variations in battery operation at a constant current rate, statistic-based HIs provide SOH insights from a different perspective. These HIs analyze the entire battery operation history (not just charge curves), including Ah throughput, vehicle mileage, time duration of battery operating at specific temperature ranges, SOC, voltage, current, etc. Statistic-based HIs are widely stored as histograms for onboard data storage to save power and memory [15]. A few studies have proposed using statistic-based HIs for both SOH estimation and aging trajectory prediction. You et al. [36] apply a K-means clustering algorithm to refine histogram data and estimate battery SOH using a feedforward neural network (FNN) model. Zhang et al. [15] propose a pipeline to predict battery aging trajectory and lifetime from statistic-calculated (e.g. average, variance, skewness, etc.) histogram data. The performance of several machine learning models (i.e. SVR, RFR, GPR, FNN) is compared in this work, demonstrating similar estimation accuracy. In [32], GPR is used to predict battery kneepoint and end of life from cumulative time histogram data. Overall, statistic-based HIs can be directly collected from any testing profiles without requiring specialized lab tests. However, since statistic-based HIs typically involve cumulative time analysis of the entire battery operation history, their correlation with SOH is often vague due to sensor noise and information loss during histogram transformation. As a result, an extensive training dataset is required for machine learning models to learn battery health information adequately.

The key original contributions of this work are summarized below:

1. A novel multi-modal knowledge fusion framework is developed, integrating the advantages of both direct-captured and statistic-based HIs. According to the authors' best knowledge, this approach is implemented for the first time in the literature and significantly improves the accuracy, robustness, and practicality of battery SOH estimation models, addressing challenges faced by traditional single-source methods.
2. The study leverages a CNN-based architecture to process the fused multi-modal HIs. This automated feature extraction and modelling technique is a novel application in the domain of battery SOH estimation.
3. The proposed approach is validated using real-world battery datasets, demonstrating its scalability, reliability, and adaptability across diverse operating conditions and battery chemistries.
4. A detailed summary and systematic comparison of existing HIs, including pre-processed, direct-captured, and statistic-based HIs, highlights the strengths and limitations of each type, offering valuable insights for further research in battery health estimation.
5. The feasibility of onboard deployment is analyzed by evaluating the computational efficiency of the proposed model on an edge computing device. Furthermore, the integration of the proposed model with cloud computing architectures is explored to address computational constraints. Additionally, the potential of applying fine-tuning strategies to enhance transfer learning performance is discussed.

The remainder of this work is organized as follows: Section 2 introduces the experimental battery datasets used in this study. Section 3 discusses the limitations and challenges of existing pre-processed, direct-captured, and statistic-based HIs in SOH estimation. In Section 4, the development methodology for the multi-modal fusion-based SOH estimator is described. Section 5 presents a comparative evaluation of the results among direct-captured, statistic-based, and multi-modal fusion SOH estimation models. Finally, the main conclusions are summarized in Section 6.

## 2. Experimental data

In this paper, two lithium-ion battery datasets that consider different materials and testing conditions are applied to evaluate the limitations of HIs and validate our proposed SOH estimation methodology. Two representative cells from each dataset are selected to illustrate the shifts of discharge capacity versus voltage ( $Q$ -V) and IC versus voltage ( $dQ/dV$ -V) curves due to cell degradation, as shown in Fig. 1. These shifts are key features targeted by both pre-processed and direct-captured HIs to extract SOH information.

### 2.1. McMaster battery dataset

This dataset was generated by our group on six 3 Ah Samsung 30 T cells with lithium nickel cobalt aluminum oxide (NCA) chemistry [37]. The cells were aged to 70 % SOH under five distinct fast-charging protocols ('CC' protocol applied to two cells) at 25 °C, namely "CC" "CC 2" "BC" "BCNP 0.1 s" "BCNP 1 s" and "BCR", as detailed in Table 2 and Fig. S1. For the aging test stage, each cell was charged with the corresponding fast charging protocol from 10 % SOC to 80 % SOC, then discharged back to 10 % SOC using drive cycle profiles (e.g. "UDDS"

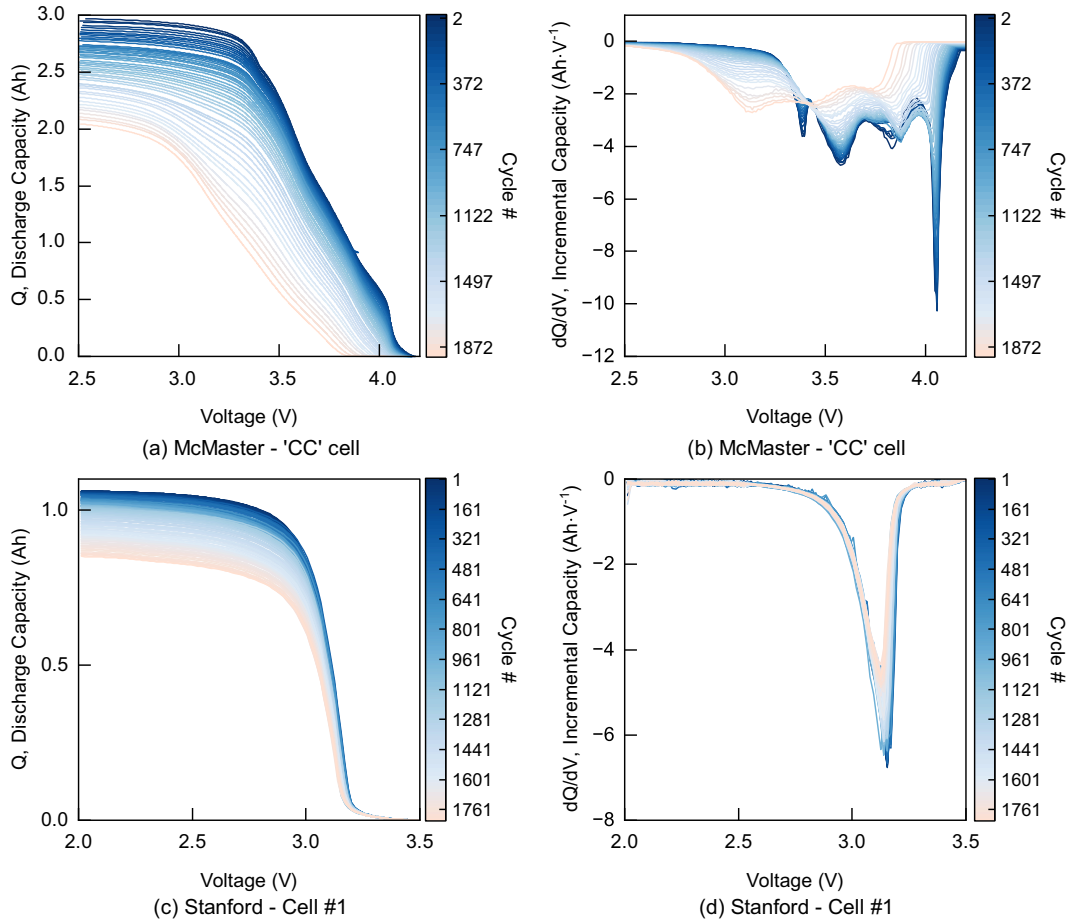


**Fig. 1.** Shifts of voltage and IC curves at a constant current rate due to cell degradation. (a) Discharge capacity and (b) incremental capacity versus voltage curves under 0.5C-rate discharge operation for the 'CC' cell in the McMaster battery dataset. The colour of each curve is interpolated by the battery cycle number, as is done throughout the work. (c) Discharge capacity and (d) incremental capacity versus voltage curves under 4C-rate discharge operation for the cell #1 in the Stanford dataset. Cells were discharged from a fully charged state to the cut-off voltage (2.5 V for the McMaster dataset and 2.0 V for the Stanford dataset), with discharge capacity values at the cut-off voltage defined as the SOH label in this study.

**Table 2**  
15 min fast charge test protocols for the McMaster dataset.

Cell	Description	Fast charge test profile
		Full name
"CC"	Constant current	2.8C-rate CC charge
"CC 2"	Constant current 2	2.8C-rate CC charge
"BC"	Boost constant current	5 min 4C-rate + 10 min 2.2C-rate
"BCNP 0.1 s"	Pulse boost protocol with 0.1 s negative pulse	1.9 s 4.323C-rate and 0.1 s -2.162C-rate for 5 min + 1.9 s 2.324C-rate and 0.1 s -1.189C-rate for 10 min
"BCNP 1 s"	Pulse boost protocol with 1 s negative pulse	1 s 4.323C-rate and 1 s -2.162C-rate for 5 min + 1 s 2.324C-rate and 1 s -1.189C-rate for 10 min
"BCR"	Pulse boost protocol with rest	1.9 s 4.323C-rate and 0.1 s rest for 5 min + 1.9 s 2.324C-rate and 0.1 s rest for 10 min

“HWFET” “LA92” “WLTP”, etc.) to simulate cell degradation in electric vehicle applications. Characterization tests, including capacity and hybrid pulse power characterization (HPPC) tests, were performed at each SOH checkpoint to assess battery capacity fade and resistance increase due to degradation. We define the SOH metric as the discharge capacity measured at a 0.5C-rate from a fully charged state to the cut-off voltage of 2.5 V in this dataset, as follows:

$$\text{SOH} = Q_i/Q_0(\%) \quad (1)$$

where  $Q_0$  is the nominal capacity when the battery is fresh and  $Q_i$  is the capacity at a certain cycle  $i$ . Since  $Q_0$  is a constant value, so  $Q_i$  alone can also be used to identify battery SOH level.

## 2.2. Stanford battery dataset

This dataset was created by the Massachusetts Institute of Technology and Stanford University [38]. 124 lithium ion phosphate (LFP) cells (A123, model APR18650M1A) with a nominal capacity of 1.1 Ah were tested at an ambient temperature of 30 °C. These cells underwent a range of fast-charging protocols denoted as ‘C1(Q1)–C2’ until 80 % SOH. Under these protocols, the cells were initially charged at a constant current, C1, up to a specified SOC, Q1. This was followed by charging at a different constant current, C2, until reaching 80 % SOC. Finally, the cells were fully charged using a 1C-rate CCCV profile. For discharging, all cells were discharged at a 4C-rate to a cut-off voltage of 2.0 V. The discharge capacity recorded during the 4C-rate discharge step serves as the SOH metric for this dataset. Details regarding the naming of cells in the Stanford dataset used in this work are provided in Table S1 in the appendix.

## 3. Problem statement of existing HIs

### 3.1. Pre-processed and direct-captured HIs can be misleading

As discussed, most pre-processed and direct-captured HIs aim to extract battery SOH information by quantifying or leveraging machine learning to identify shifts in the shape and position of the voltage or IC curves under constant current conditions. These HIs have an assumption that cells with the same remaining capacity (SOH) will have the same voltage or IC curves.

A case study from the McMaster dataset is presented in Fig. 2(a). When identifying the most similar voltage curve from the ‘CC’ cell at various SOH levels to the ‘BCR’ cell at 86.7 % SOH, the ‘CC’ cell’s curve at 90.1 % SOH is incorrectly identified as the most similar one, instead of the expected ‘CC’ cell curve at 86.7 % SOH. Additionally, Fig. 2(c) highlights that voltage curves of six differently aged cells at the same 80 % SOH (ending with the same discharge capacity at the cut-off voltage) exhibit significant variations in shape. This phenomenon is also evident in IC curves since they are generated from the voltage curves. In Fig. 2(b), the IC curve of the ‘CC’ cell at 89.1 % SOH is identified as the most similar one to the ‘BCR’ cell at 86.7 % SOH, instead of the expected ‘CC’ cell’s 86.7 % SOH one. Similarly, Fig. 2(d) shows that IC curves of these six cells at the same 80 % SOH display considerable shape differences. These mismatches between SOH and the shape of voltage or IC curves highlight the potential for pre-processed and direct-captured HIs to mislead SOH estimation. This risk worsens when only partial curves are usually used for SOH estimation in real-world applications, as mismatches can be more pronounced in specific curve ranges.

The mismatches between SOH and the shape of voltage or IC curves are primarily attributed to the inconsistent aging behaviours of cell capacity and resistance. As illustrated in Fig. 2(e), the resistance measured from a 0.5C-rate charge pulse shows diverse trends among six cells as

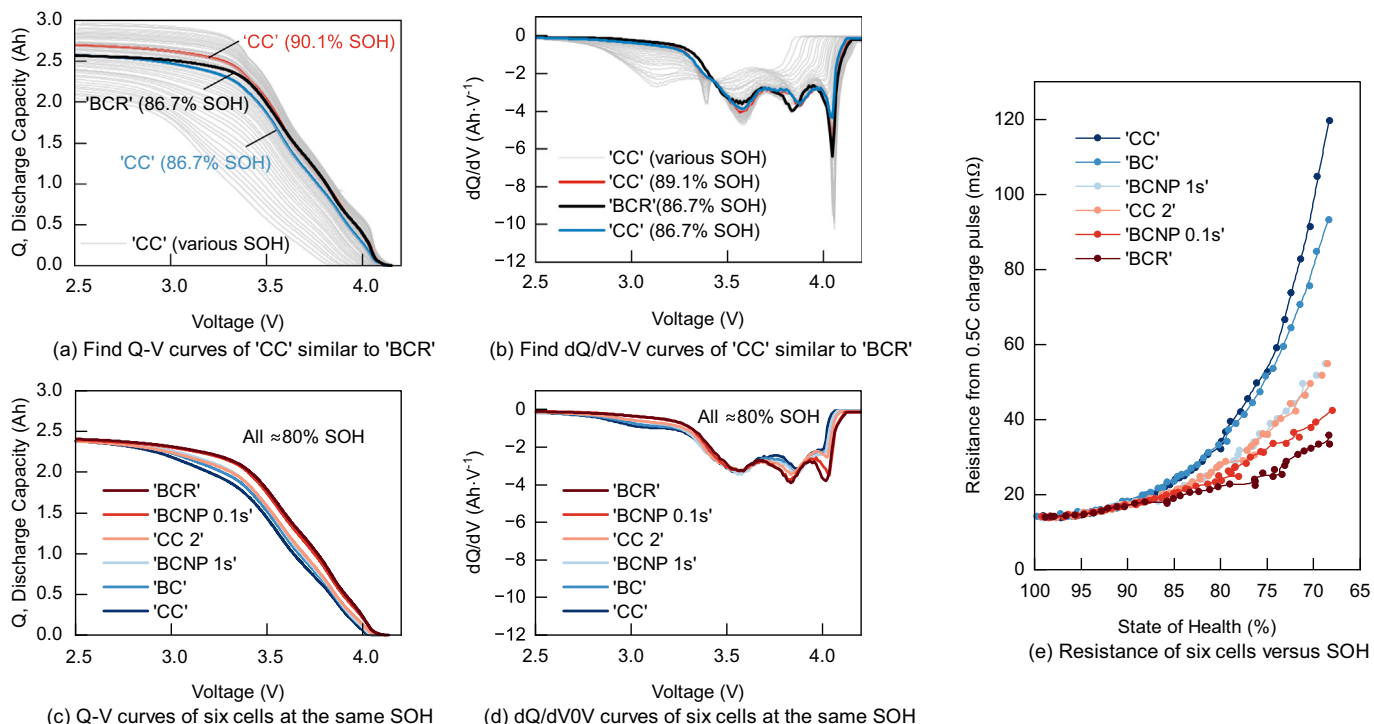


**Fig. 2.** Mismatches between SOH and 0.5C-rate discharge operation voltage (Q–V), IC ( $dQ/dV$ –V), and resistance curves among cells from the McMaster dataset. (a) The most similar voltage curve among the ‘CC’ cells at various SOH levels to the ‘BCR’ cell at 86.7 % SOH is identified as the 90.1 % SOH one instead of the expected 86.7 % SOH one. (b) The most similar IC curve among the ‘CC’ cell at various SOH levels to the ‘BCR’ cell at 86.7 % SOH is identified as the 89.1 % SOH one, instead of the expected 86.7 % SOH one. (c) Voltage curves of six cells at the same SOH level. (d) IC curves of six cells at the same SOH level. (e) Resistance measured from 0.5C-rate charge pulse for six cells during cell aging tests. It highlights that pre-processed and direct-captured HIs generated from these curves may provide misleading SOH estimation. Note: The similarity identification shown in (a) and (b) utilizes the dynamic time warping (DTW) method.

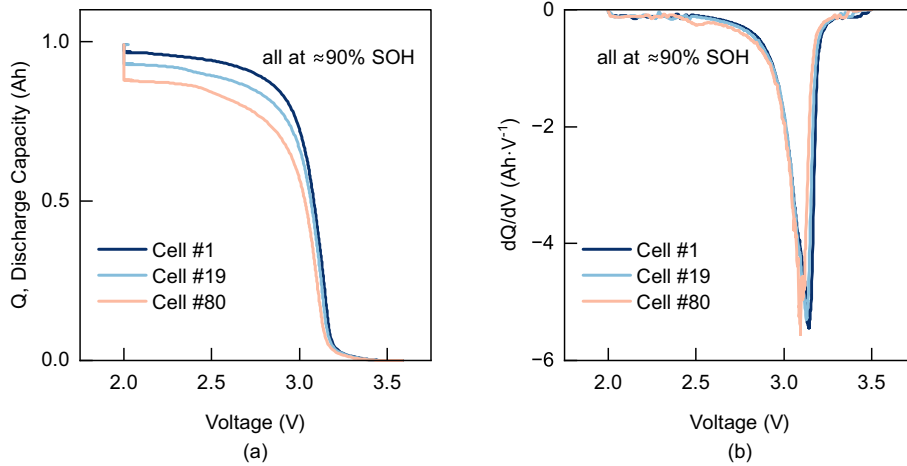


**Fig. 3.** Mismatches between SOH and 4C-rate discharge operation voltage (Q–V) and IC ( $dQ/dV$ –V) curves among three representative cells: cell #1, #19, and #80 from the Stanford dataset. (a) Voltage curves for three cells at the same 90 % SOH. (b) IC curves for three cells at the same 90 % SOH. It highlights that the mismatch between SOH and voltage or IC curves is commonly observed in different battery test datasets. Note: The 4C-rate discharge process includes a cut-off current (C/50) at the constant voltage stage, which is why vertical curves are recorded near the cut-off voltage.

they age. This variation can be attributed to different degradation modes across the cells [6]. For instance, the ‘CC’ cell may experience a more pronounced increase in impedance, while the ‘BCR’ cell may suffer more from the loss of lithium inventory and active material degradation.

It should be noted that only the partial voltage curve corresponding to a discharge capacity range of 0–2 Ah is used for the similarity analysis in Fig. 2(a). This approach avoids disclosing SOH information directly (discharge capacity at the cut-off voltage) if the entire voltage curves are used. Entire IC curves are used for similarity analysis. To perform a similarity comparison between two curves with different lengths as shown in Fig. 2(a) and (b), a dynamic time warping (DTW) algorithm [39] is applied. The DTW computes the distance by aligning corresponding points in both curves while minimizing the accumulated distance. Given two curves  $A = \{(x_1, y_1), (x_2, y_2), \dots, (x_N, y_N)\}$  and  $B = \{(u_1, v_1), (u_2, v_2), \dots, (u_M, v_M)\}$ , the DTW distance  $D(i, j)$  between two curves is given by the recurrence relation:

$$D(i, j) = d((x_i, y_i), (u_j, v_j)) + \min \begin{cases} D(i-1, j), \\ D(i, j-1), \\ D(i-1, j-1) \end{cases} \quad (2)$$

where  $d((x_i, y_i), (u_j, v_j)) = \sqrt{(x_i - u_j)^2 + (y_i - v_j)^2}$  is the Euclidean distance between the  $i$ -th point of curve A and the  $j$ -th point of curve B.  $D(N, M)$  serves as the metric for quantifying the similarity between two voltage curves or IC curves. DTW method was used to locate the most similar Q–V and IC curve from ‘CC’ cell to ‘BCR’ cell in Fig. 2(a) and (b).

The mismatches between SOH and voltage or IC curves are also observed in the Stanford dataset, as shown in Fig. 3. It highlights that this is a common issue where pre-processed and direct-captured HIs may mislead SOH estimation. In the Stanford dataset, the 4C-rate discharge process has a cut-off current (C/50) at a constant voltage stage. Therefore, vertical curves are recorded near the cut-off voltage in Fig. 3(a).

### 3.2. Statistic-based HIs require massive training data

Unlike pre-processed and directly captured HIs, statistic-based HIs do not rely on voltage or IC curves. As a result, they are not affected by the mismatch issue discussed in Section 3.1. However, statistic-based HIs, such as cumulative time histograms, cell Ah throughput, and mileage driven, exhibit a relatively weaker correlation with SOH compared to

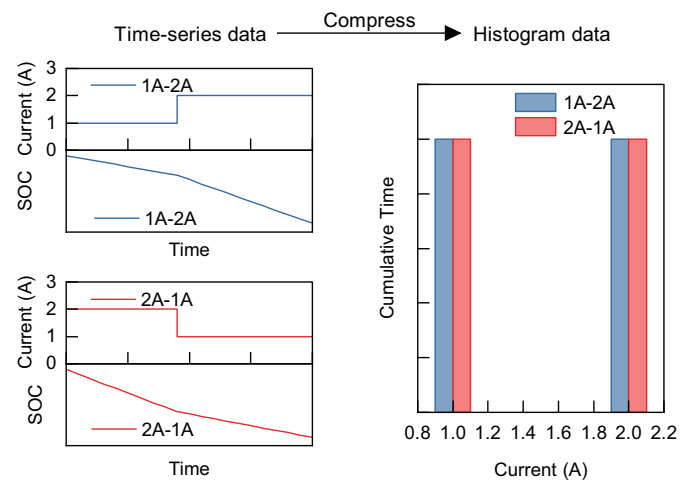
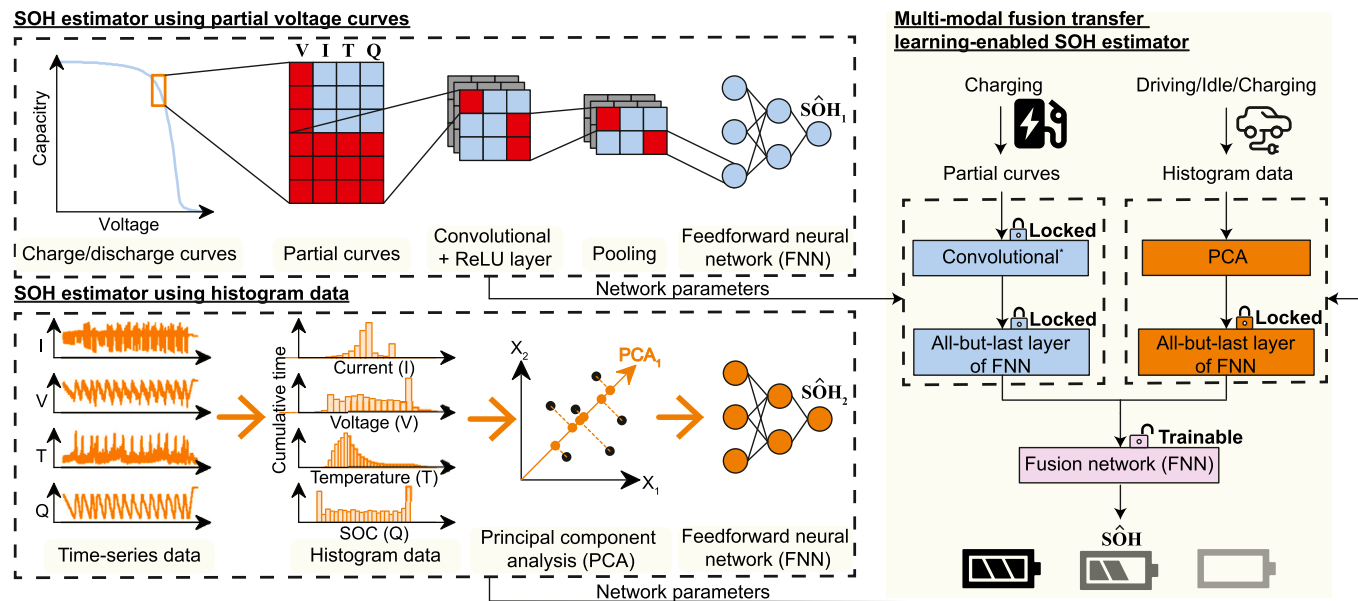


**Fig. 4.** Two pulses of 1A and 2A, applied in different sequences, yield identical cumulative time histogram results after histogram compression. This demonstrates that the influence of varying current rates applied at different SOCs is neglected in the histogram compression process.

other HIs. To enable data-driven models to extract meaningful SOH information from these features, extensive training data are required.

A common example of statistical HIs is the cumulative operational duration of a battery, such as the total time it operates at a 5 C current rate through its operation history. However, converting time-series data into cumulative histograms compresses the data, leading to significant information loss, especially regarding the sequence of battery operations. For example, as illustrated in Fig. 4, distinct operational pulse sequences can appear identical after histogram compression, losing crucial operational patterns. The sequence of operations is vital for data-driven models to understand battery health, as the aging impact of operating at low or high SOC can vary significantly, yet this detail is absent from histogram data. While features like  $SOC^*I$  (state of charge multiplied by current) [40] can partially recover the lost information, statistical HIs still show weaker correlations with SOH compared to features derived from voltage or IC curves. To address the limitations of histogram compression, data-driven methods require large



\*'Convolutional' includes Convolutional layer, ReLU layer and Pooling layer.

**Fig. 5.** Workflow of the proposed multi-modal knowledge fusion based SOH estimation method. The network dimensions shown in this figure are for conceptual illustration only and do not represent the actual structure used in this study. Details about the network structure can be found in Fig. S2 in the Appendix.

and diverse training datasets to effectively extract SOH information [15,32].

#### 4. Methods

In this section, a multi-modal fusion-based SOH estimation model is proposed, which transfers and refines the knowledge extracted from both CNN-based SOH estimator using partial voltage curves and FNN-based SOH estimator using histogram data, as illustrated in Fig. 5.

##### 4.1. CNN-based SOH estimator using only partial charge curves

Accurate SOH estimation depends on selecting relevant input data that effectively capture battery degradation. Instead of relying on pre-processed HIS through a tedious feature engineering process, this study applies deep learning techniques to automatically extract meaningful features from raw battery operation data. Raw operation data refer to partial voltage curves corresponding to the selected SOC range. Current and temperature curves are added to ensure the model's robustness across different C-rate and ambient temperature conditions.

A critical aspect of this approach is the selection of an appropriate SOC range for partial curves. To balance accuracy and practicality, a 14 % SOC range (further discussed in Section 5.2) during a constant current stage is selected: 1000 out of 7200 s for the McMaster dataset from a 0.5C-rate discharge profile and 125 out of 900 s for the Stanford dataset from a 4C-rate discharge profile. This range is sufficient for extracting SOH-related features while ensuring applicability across real-world scenarios, including electric vehicles and portable electronic devices. Furthermore, partial curves near the cut-off voltage are excluded to prevent SOH label leakage, which could compromise model generalization.

Extracting SOH information from partial battery operation curves can be framed as a task of identifying the most similar pattern within the training dataset that corresponds to the input partial curves, as is done in Section 3.1, using the DTW algorithm. However, traditional algorithms (e.g. DTW method) only measure the similarity between input and training data instead of inherently learning battery aging behaviour reflected in the spatial variation on operation curves. Therefore, they

heavily rely on the quality of prepared training data and struggle to handle uncertainty and noise. Also, traditional algorithms can only be used to estimate SOH, while machine learning algorithms have the potential to predict battery aging behaviour into the future [38].

Among various machine learning techniques, CNN is well-recognized as a powerful tool to extract and refine information from image signals [31]. Thanks to the unique design of convolutional and pooling layers, CNNs can capture patterns regardless of their position in the input. This capability is a significant advantage over FNN in battery SOH estimation tasks, as partial curves can be selected over any SOC range.

The structure of the CNN-based SOH estimator can be found in Fig. 5 within the dashed box labelled 'SOH estimator using partial voltage curves' and further detailed (e.g. neural and kernel size) in Fig. S2. CNN consists of a convolutional layer, a pooling layer, and a fully connected layer. The convolutional layer is responsible for feature extraction by sliding kernels (filters) across the input data, performing a convolution operation between the input  $I$  and the kernel  $K$  to generate feature maps  $F$ . A 1-dimension convolutional layer with three input channels (i.e. voltage, current, and temperature) is used, which can be mathematically expressed as:

$$F_i = \sum_{c=0}^{C_{in}-1} \sum_{m=0}^{M-1} w_{m,c} \cdot x_{i+m,c} + b_c \quad (3)$$

where  $F_i$  represents the feature map at position  $i$ ,  $C_{in}$  denotes the size of input channel,  $M$  refers to the size of the kernel,  $w$  and  $b$  represent the weight and bias, respectively.

Rectified linear unit (ReLU) layer is used as an activation function to introduce nonlinearity into the model, which can be represented as:

$$\text{ReLU}(x) = \max(0, x) \quad (4)$$

The Max pooling layer is used to reduce the spatial dimensions of the feature maps while retaining important SOH information:

$$y(i) = \max(x(i), x(i+1), \dots, x(i+k)) \quad (5)$$

where  $k$  is the length of the sliding window.

**Table 3**  
Histogram features construction.

	Histogram bin features*	
	McMaster	Stanford
Current (A)	–35:1:35	–10:0:1:10
Voltage (V)	2.5:0.1:4.2	1.5:0.1:4
Temperature (°C)	20:1:45	20:1:40
Capacity (Ah)	0:0:03:3	0:0:1:1.1
QxI (Ah A)	–105:1:105	–11:0:1:11
Total features	427	560

\* Values follow the format: minimum:step:maximum.

Fully connected layers (i.e. FNN) are used at the end to flatten and refine information collected within feature maps:

$$y = \text{ReLU}(wx + b) \quad (6)$$

#### 4.2. FNN-based SOH estimator using only histogram data

Partial curve data provide insights into short-term charge/discharge behaviour but may not fully capture long-term degradation effects arising from different operation conditions. To complement partial curve-based features, this study incorporates histogram-based features, which represent the cumulative operational history of the battery. Unlike voltage and IC curves, which focus on specific charge events, histogram features aggregate battery operation data over extended periods, offering a broader view of degradation trends. If only partial charging or discharging data are available, histogram-based HIs can still function, though their performance may be compromised due to the limited information embedded in operational data.

Histogram-based HIs include current (I), voltage (V), temperature (T), discharged coulomb since fully charged (Q), and discharged coulomb times current (Q × I, same as SOC \* I [40]), binned over defined ranges, as detailed in Table 3. These features contain valuable battery degradation information [15], including deep of discharge (DOD), accumulated cycle time, accumulated Ah throughput, etc. Structuring histogram-based HIs significantly reduces the number of data points, making real-time data collection feasible.

Histogram-based HIs' applicability is not restricted to controlled laboratory conditions. In real-world scenarios, histogram features can be continuously accumulated from battery operation history under varying drive cycles, dynamic loads, and different charging patterns. This makes histogram-based SOH estimation practical for real-world BMS implementations, requiring only continuous data logging within predefined margins without the need for strictly controlled conditions.

Despite their advantages, we find two challenges in using a data-driven model to extract SOH information:

1. The histogram data are sparse, as the feature ranges are defined to cover all possible values, while the battery rarely operates within some of these ranges. These redundant features can lead to overfitting and increased model complexity.
2. The cumulative time for each histogram feature lacks a defined boundary, making the values to grow indefinitely during real-time recording.

Therefore, principal component analysis (PCA) [41] is employed in this work to reduce the dimensionality of histogram features while retaining as much information as possible for better machine-learning model performance. PCA is a powerful unsupervised learning tool widely used for dimensionality reduction and feature extraction. It works by projecting the data onto a new coordinate system where the axes (principal components) are chosen to maximize the variance of the projected data. These axes correspond to the eigenvectors of the covariance matrix of the data, and the variance explained by each component corresponds

to the eigenvalues. PCA first computes the covariance matrix  $C$  of input features. Then, eigenvalue decomposition is applied by solving the eigenvalue problem for  $C$ :

$$Cv_i = \lambda_i v_i \quad (7)$$

where  $\lambda_i$  represents the eigenvalues and  $v_i$  are the corresponding eigenvectors; both are sorted in descending order. Then, top  $k$  eigenvectors corresponding to the  $k$  largest eigenvalues are selected to for the projection matrix  $P$ ,

$$P = [v_1, v_2, \dots, v_k] \quad (8)$$

and the original features  $X$  are projected to PCA space  $X_{PCA}$  by:

$$X_{PCA} = XP \quad (9)$$

It should be noted that the top  $k$  eigenvectors are selected by achieving the threshold reconstruction level  $t$  (i.e. 99 %) in this work:

$$\frac{\sum_{i=1}^{\text{dimension of } X_{PCA}} \lambda_i}{\sum_{i=1}^{\text{dimension of } X} \lambda_i} \geq t \quad (10)$$

Applying PCA transformation features the original 427 histogram features to just 12 for the McMaster dataset and from 560 to 69 for the Stanford dataset. This significantly lowers the complexity of the required machine-learning model and mitigates the risk of overfitting.

To estimate SOH from the PCA-transformed histogram HIs, an FNN, as shown in (6), is then used to estimate SOH using the prepared histogram data, and the structure can be found in Fig. 5 and detailed in Fig. S2. A dropout layer (with a probability of 0.2) is introduced after the fully connected layers in the histogram-based SOH estimator to combat overfitting and improve generalization.

#### 4.3. Multi-modal fusion-based SOH estimator via transfer learning from both partial charge and histogram data

Fig. 5 illustrates the scheme of the proposed multi-modal knowledge fusion-based SOH estimation model. As discussed in Section 3, relying solely on direct-captured HIs or statistic-based HIs for SOH estimation presents inherent challenges, namely, the mismatch between SOH and voltage curves, as well as the weak correlation between SOH and histogram-based HIs. To improve SOH estimation performance, we propose applying a multi-modal knowledge fusion technique to train a model that incorporates both types of HIs, described as follows:

1. **Independent SOH Estimation Models:** Two separate SOH estimation models are first trained, one using partial voltage curves (processed via a CNN) and another using histogram data (processed via an FNN). These models gain the ability to extract SOH-relevant features from their respective input data sources through model training.
2. **Knowledge Transfer and Fusion:** The learned knowledge from both models are then transferred to a new fusion model via the outputs of their all-but-last layers, where their parameters are copied and locked during training. This ensures that the pre-trained models retain their ability to extract SOH-relevant features while providing complementary information to the final fusion network.
3. **Automatic Weight Determination:** The final fusion FNN network collects and processes the outputs from both independent SOH estimators. During training, this FNN automatically determines the relative contribution (i.e. weight) of each HI type based on its effectiveness in minimizing the overall SOH estimation error. This approach ensures that the fusion process is adaptive and can leverage the strengths of each HI type based on dataset characteristics and training conditions. Details about the network structure can be found in Fig. S2.

The learned weights reflect the importance of each HI source under different conditions. For instance, if histogram data are sparse or less informative, the fusion model may assign a higher weight to the partial voltage curve estimator. Conversely, in scenarios where voltage curve features are less reliable (e.g. due to the mismatch between SOH and voltage curves), the model can increase reliance on the histogram-based estimator. This adaptive weighting mechanism allows the multi-modal fusion approach to achieve superior estimation performance compared to single-source models.

By integrating knowledge from both HIs, the proposed method overcomes individual limitations and significantly enhances estimation accuracy. This approach is particularly beneficial for real-world applications, where available data sources may vary in quality and completeness.

It should be noted that if pre-trained models exhibit unacceptable performance (e.g. a model trained using a histogram with a very limited data size), it is not necessary to transfer and lock their network parameters during the training of the multi-modal fusion model, as their pre-learned knowledge would not provide significant value. For instance, we did not lock the part of the histogram-based SOH estimator's parameters during the training of the multi-modal fusion model for the McMaster dataset and Stanford (4 cells) case, as the performance of these pre-trained histogram-based models was too poor.

## 5. Results and discussion

Several experimental cases are designed and discussed in this section. The training hyperparameters and data split used throughout this work are presented in Tables 4 and 5, respectively. The machine learning models were developed in a Python 3 environment using the PyTorch library [42], while data analysis and pre-processing were conducted in MATLAB. The cross-validation process and model training were executed on a server with four NVIDIA A100 GPUs.

To ensure optimal model performance and training stability, we systematically selected key hyperparameters based on empirical analyses and cross-validation results. The following criteria guided the selection process:

1. **Learning Rate and Adaptation Strategy:** The initial learning rate was set to 0.0001, determined through a grid search within the range of  $10^{-5}$ – $10^{-2}$ . This range was chosen to balance convergence speed and stability. Additionally, a learning rate scheduler was implemented, reducing the learning rate by a factor of 0.1 after 1000 epochs if the validation loss does not improve. This adaptive approach improved convergence and prevented the model from getting stuck in local minima.

**Table 4**  
Network training hyper-parameters.

Hyper-parameters	Values
Mini-batch size	100
Validation frequency	3
Validation patience	100
Initial learning rate	0.0001
Learning rate drop period	1000
Learning rate drop factor	0.1

**Table 5**  
Data split for machine learning model training.

Data split		
	McMaster dataset	Stanford dataset*
Training	'BC' 'CC' 'BCR' 'BCNP 1 s'	Cell #1 to #100
Testing	'CC 2' 'BCNP 0.1 s'	Cell #101 to #124

\* See Table S1 for more information.

2. **Batch Size Considerations:** We selected a batch size of 100 after evaluating multiple options (e.g. 50, 200, 500). Smaller batch sizes introduced instability due to higher variance in gradient updates, while larger batch sizes resulted in increased memory consumption without a proportional improvement in performance. The final choice provided a balance between computational efficiency and generalization. Based on our observations, hyperparameters such as learning rate and batch size have a limited impact on final model performance.
3. **Cross-Validation and Early Stopping** A five fold cross-validation strategy was employed to optimize hyperparameters and evaluate model robustness. To prevent overfitting and unnecessary training, early stopping was implemented with a patience threshold of 100 epochs, terminating training when the validation loss did not improve for 100 consecutive epochs.
4. **Optimizer and Regularization:** The Adam optimizer was selected for its adaptive learning rate properties, which helped maintain stable convergence across different training conditions. To further mitigate overfitting, we applied dropout regularization (dropout rate = 0.2) in the histogram-based SOH estimator, as histogram features are high-dimensional and may introduce redundancy.
5. **Neural Network Architecture Tuning:** In addition to hyperparameter tuning, we optimized network depth and neuron configurations using a grid search approach, ensuring the architecture was neither too simple (underfitting) nor excessively complex (overfitting), as detailed in Section 5.1. The final architecture was chosen based on minimizing the cross-validation error, as detailed in Fig. S2.

### 5.1. Network architecture tuning and model selection

The model structure and sizing used in Fig. 5 is determined through comprehensive comparison and analysis, summarized into three main concerns: (a) Is the network size used in this work optimal? (b) Is CNN necessary for partial voltage curve based SOH estimator? (c) Is PCA necessary for histogram-based SOH estimator?

Optimizing the size of networks is crucial, as an under-sized network may lead to under-fitting, while an over-sized network can result in over-fitting. Both scenarios negatively impact model performance. Furthermore, it is only fair to compare two model structures (e.g. CNN vs. FNN) under their respective optimal configurations. Therefore, a  $K$ -fold cross-validation network sizing fine-tuning process was conducted for all models used in this work, described as follows:

1. The battery dataset is split into training and testing sets. The training set is shuffled and further divided into several equally-sized folds (5 folds are used in this work).
2. The model is trained on  $k-1$  folds and validated on the remaining fold. This process is repeated  $k$  times, each time using a different fold as the validation set and the rest as the training set.
3. The network sizing (e.g. the number of layers or neurons) is adjusted iteratively with logarithmic grid search (i.e.  $2^i$ ), and the model is re-trained and validated for each configuration across all folds.
4. The root mean square error (RMSE) is calculated for each fold. The optimal network configuration is selected by minimizing the mean RMSE across folds with the same network setup.

For the partial voltage curves based SOH estimator, the CNN is expected to outperform the FNN due to its well-established ability to extract patterns from image-based features, i.e. partial voltage curves in this case. The results of  $K$ -fold cross-validation analysis for both FNN and CNN on partial voltage curves are shown in Fig. 6(a). The CNN consistently outperforms the FNN, demonstrating lower cross-validation errors on the same training dataset across nearly all configurations of

learnable parameters. The optimal network sizes for FNN and CNN are selected by minimizing the cross-validation error while maintaining a similar model size for fair comparison. By evaluating these two models with optimal sizing on the testing sets from the McMaster dataset, the CNN achieved a root mean square percentage error (RMSPE) of 2.29 %, outperforming the FNN, which recorded an RMSPE of 2.87 %. Therefore, CNN is selected for the SOH estimation using partial voltage curves.

For the histogram based SOH estimator, although various machine learning models, such as SVR, RFR, and GPR, may serve as alternatives to the neural networks used in this work, we decided to focus our discussion mainly on neural networks. This is because traditional machine learning models, including SVM, RFR, and GPR, are not well-suited for the transfer learning approach applied in this study. Neural networks enable flexible transfer of rich, pre-learned knowledge through the middle layers of a pre-trained model, whereas traditional models only allow the use of estimated SOH values as pre-learned knowledge, limiting the depth of information transfer. Additionally, in [15], different models, including SVM, RFR, GPR, and FNN, were applied to extract battery health information from statistically based HIs. The FNN outperformed the other models in terms of accuracy and computational efficiency. Therefore, FNN was selected for the task of SOH estimation using histogram data in this work.

We evaluate the improvement from PCA on histogram-based SOH estimation by training two FNN-based SOH estimators: one with PCA transformation and one without it applied to histogram data. As shown in Fig. 6(b), *K*-fold cross-validation processes were applied to optimize the network sizing for both SOH estimators with and without PCA. When tested on the Stanford dataset, the SOH estimator using PCA-transformed histogram achieved an RMSPE of 1.03 %, significantly outperforming the estimator without PCA, which yielded an RMSPE of 3.56 %. Additionally, the model architecture using PCA (with only 19,329 learnable parameters) is approximately ten times smaller in size compared to the non-PCA model (with 184,833 learnable parameters), highlighting its computational efficiency and suitability for deployment in resource-constrained environments. These compelling results strongly emphasize the necessity of integrating PCA into the proposed model to achieve superior estimation accuracy, reduce model complexity, and improve scalability.

In this study, network sizing was optimized solely based on model accuracy, ensuring a fair comparison across different architectures. Computational efficiency was not explicitly considered, as the primary objective was to establish optimal accuracy for SOH estimation. Furthermore, the algorithm executes in less than 20 ms and only needs to be run once per charge/discharge cycle at most, so computational complexity is not a very important factor in network sizing.

It should be noted that similar network sizing optimization processes were applied to all networks utilized in this work, and the optimized structures are illustrated in Fig. S2. The optimization results indicate that adding more complexity to the model structure provides no additional benefit, as the network sizing is already an optimal choice. This demonstrates that the improvement achieved with the multi-modal fusion method is from including additional information through feature combination rather than from increased model complexity.

## 5.2. Effect of partial profile SOC window on SOH estimation

The performance of a direct-captured HIs based SOH estimator heavily depends on the length and position of the partial curves. To demonstrate the impact of these factors, we trained multiple models to evaluate how the length and position of partial profiles affect the accuracy of a CNN-based SOH estimator using direct-captured HIs, as shown in Table 6. It should be noted that the sizes of the networks used for this comparison were optimized according to the cross-validation error.

A longer partial curve is expected to contain more pronounced SOH information; an extreme example is that an entire voltage curve directly indicates SOH. As shown in Table 6, we selected four different partial curves with SOC lengths ranging from 7.2 % to 42 % and trained 8 CNN-based SOH estimators on the McMaster and Stanford datasets in total. On the Stanford dataset, it is evident that providing longer partial curves improves the estimator's accuracy. For instance, the estimator achieves an RMSPE of 1.22 % when using a 42 % SOC-length curve, compared to an RMSPE of 2.80 % when using a 7.2 % SOC-length curve. For the McMaster dataset, the estimation accuracy improves as the partial curves become longer. However, the trend is less pronounced due to the smaller training dataset size (192 recorded aging cycles) compared to the Stanford training dataset (73,743 recorded aging cycles). Dividing

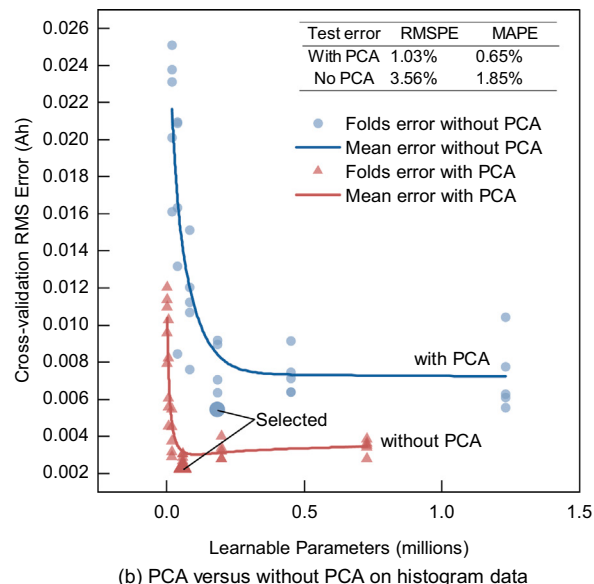
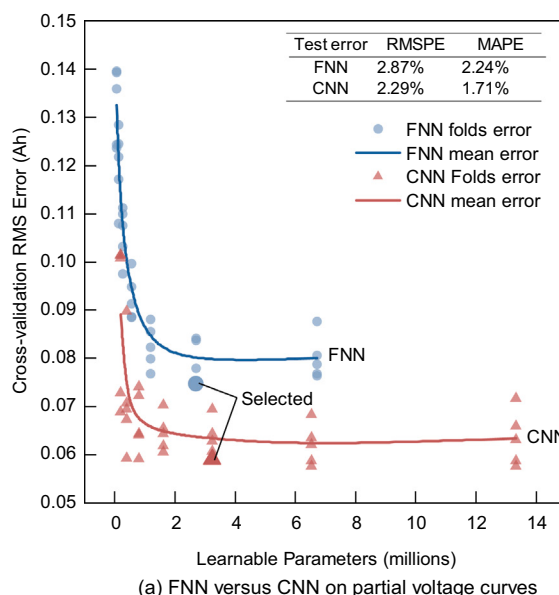


**Fig. 6.** Results of network sizing tuning process using *K*-fold cross validation. (a) Network sizing tuning of FNN and CNN-based SOH estimators using partial voltage curves on the McMaster dataset, showcasing the superior SOH estimation accuracy of CNN compared to FNN. (b) Network sizing tuning of SOH estimators using histogram data with and without PCA on the Stanford dataset, highlighting the improved estimation accuracy and reduced model complexity achieved by the PCA transformation.

**Table 6**

SOH estimation using only CNN and partial voltage curves of different SOC ranges and locations.

SOC location	McMaster		Stanford	
	RMSPE	MAPE	RMSPE	MAPE
100 %–86 %	2.65 %	2.02 %	4.78 %	2.94 %
86 %–72 %	2.42 %	1.59 %	1.30 %	0.94 %
72 %–58 %	2.68 %	2.03 %	1.25 %	0.91 %
58 %–44 %	2.41 %	1.88 %	0.85 %	0.66 %
44 %–30 %	1.64 %	1.36 %	1.04 %	0.75 %
30 %–16 %	1.38 %	1.24 %	1.32 %	0.95 %
SOC length <sup>*</sup>	McMaster		Stanford	
	RMSPE	MAPE	RMSPE	MAPE
7.2 %	2.33 %	1.62 %	2.80 %	1.76 %
14 %	2.29 %	1.71 %	2.11 %	1.23 %
28 %	2.16 %	1.48 %	1.54 %	1.10 %
42 %	2.00 %	1.57 %	1.22 %	0.87 %

\* Errors are calculated on all SOC ranges.

voltage curves into shorter partial curves can generate more training points. Consequently, the results for the McMaster dataset are influenced by the trade-off between partial curve length and training data size. This issue is not present in the Stanford dataset, as its significantly larger dataset size eliminates such limitations. Overall, we selected 14 % SOC length throughout the rest of this work, considering the trade-off between accuracy and practicality in real life.

To investigate the impact of SOC locations of partial curves on SOH estimation, we grouped the estimation results into various SOC ranges, as summarized in **Table 6**. For the McMaster dataset, it is evident that SOC ranges closer to the cut-off voltage provide better SOH estimation accuracy. This observation aligns with the voltage curves shown in **Fig. 2(c)**, where the variance between voltage curves diminishes as they approach the cut-off voltage. For the Stanford dataset, when the input partial curves are within the SOC range of 100 %–86 %, the CNN-based SOH estimator fails to provide accurate SOH estimations, yielding an RMSE of 4.78 %. This inaccuracy arises due to the similarity of voltage curves near the fully charged state, as shown in

**Fig. 3(a)**. Such similarity challenges the machine learning model in accurately inferring SOH from partial voltage curves. Another observation is that when tested on the Stanford dataset, the most accurate cases happen when input partial curves are located at the SOC range of 58 %–44 % instead of being located closest to the cut-off voltage as observed in the McMaster dataset. This difference arises because, in the McMaster dataset, SOH is defined based on the discharge capacity following the CC discharge profile. In the Stanford dataset, however, SOH is defined from the discharge capacity after the CCCV discharge profile. The additional CV stage in the Stanford dataset, depicted in **Fig. 3(a)**, introduces greater complexity, making it more challenging for the SOH estimator to infer SOH from partial voltage curves accurately.

### 5.3. Enhancing SOH estimation through multi-modal knowledge fusion

#### 5.3.1. Accuracy improvement achieved for two representative cells

The estimation results of three SOH estimators are first presented on two representative cells, namely the 'CC 2' cell from the McMaster dataset and the cell # 104 from the Stanford dataset, as shown in **Fig. 7**. For the 'CC 2' cell, as shown in **Fig. 7(a)**, the SOH estimator using partial curves and a multi-modal fusion model both achieve decent estimation accuracy. However, the histogram-based SOH estimator fails to provide accurate results due to the limited data size of the McMaster dataset (with only 192 recorded aging cycles).

In **Fig. 7(b)**, 4 out of 100 cells in the training data from the Stanford dataset were used to train models. Once again, the histogram-based SOH estimator fails to provide accurate SOH estimations due to the limited training data. However, in this case, the SOH estimator based on partial voltage curves between 100 % and 86 % SOC also struggles to deliver reliable predictions. This is due to a mismatch issue with the partial voltage curve HIs. As illustrated in **Fig. 8(a)**, the representative cell from the Stanford dataset exhibits nearly identical voltage curves in the 100 %–86 % SOC range, regardless of whether it is new (100 % SOH) or aged (80 % SOH). Consequently, estimating SOH based solely on partial voltage curves is infeasible in this scenario.

Notably, our proposed multi-modal fusion model still achieves high SOH estimation accuracy despite the limitations of the other two models. This success stems from the model's unique fusion mechanism, which

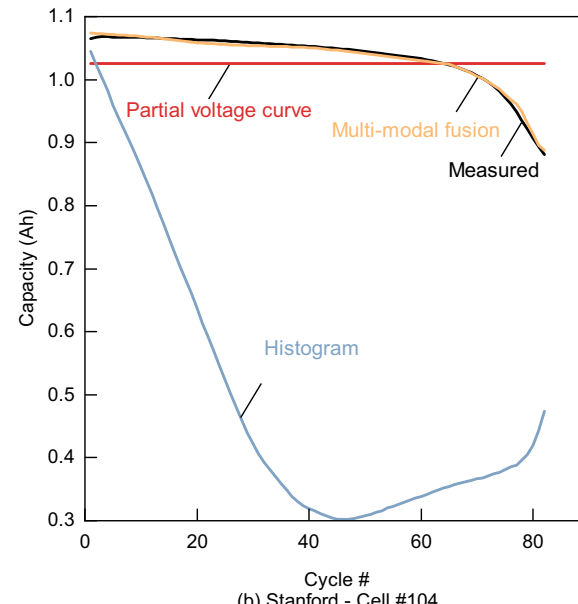
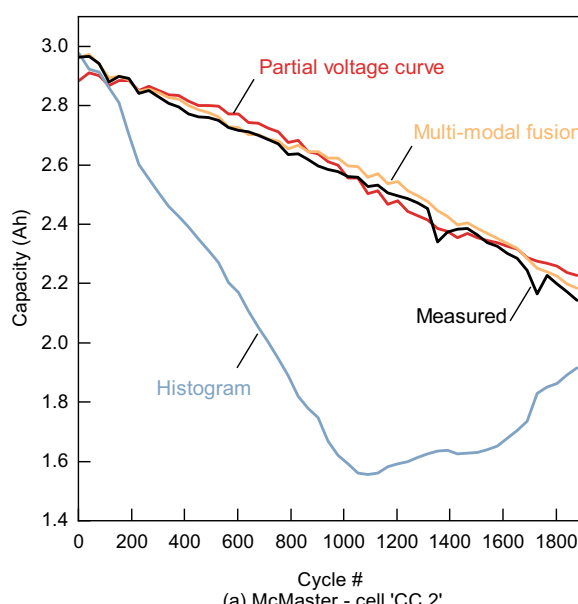


**Fig. 7.** SOH estimation results of three SOH estimators on two representative cells across aging cycles, namely the 'CC 2' cell from the McMaster dataset and the cell #104 from the Stanford dataset (training with only four selected cells). In both examples, the SOC window considered spans from 100 % SOC to 86 % SOC.

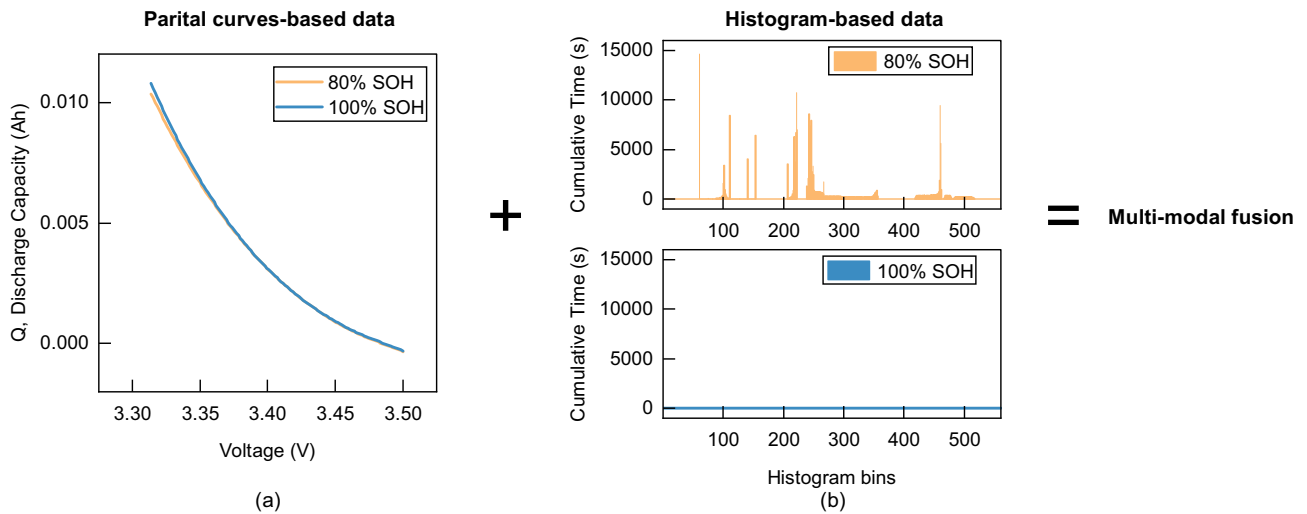


**Fig. 8.** A showcase illustrating how multi-modal fusion improves SOH estimation by combining partial voltage curves and histogram data. (a) Partial voltage curves are extracted from the Stanford-cell #101's 100 %–86 % partial 4C-rate discharge voltage curve at cycle#1 and cycle#1049. It shows that cell #101 has identical 100 %–86 % SOC partial voltage curves when at 80 % SOH compared to 100 % SOH. (b) Histogram data were recorded from the same cell. The histogram for a 100 % SOH cell is all zero because no operation is applied on the cell yet. The results highlight a critical limitation: partial voltage curves fail to provide accurate SOH information, as the selected voltage curves appear identical for the same cell at 80 % and 100 % SOH. In contrast, histogram data successfully differentiate these states, offering a clearer and more reliable SOH assessment. By integrating both types of HIs, our proposed model addresses this limitation.

**Table 7**  
SOH estimation accuracy results.

	McMaster (4 cells)		Stanford (100 cells)		Stanford (4 cells)*	
	RMSPE	MAPE	RMSPE	MAPE	RMSPE	MAPE
CNN with partial voltage curve	2.29 %	1.71 %	2.11 %	1.23 %	2.41 %	1.39 %
FNN with histogram data	27.3 %	23.1 %	1.03 %	0.65 %	52.05 %	47.47 %
Multi-modal fusion	1.36 %	1.04 %	0.74 %	0.50 %	1.40 %	1.05 %

\* Select 4 cells from 124 cells as training set (cell #2, 19, 37, 42).

integrates information from both data sources. As shown in Fig. 8, although the cell's voltage curves remain nearly identical at 100 % and 80 % SOH, its histogram-based features exhibit significant differences. In this case, the histogram data provides critical supplementary information for battery health estimation. At the same time, the partial voltage curve data address the limitation that histogram-based data alone are insufficient for training a machine learning model when the dataset size is small. This example highlights the advantages of fusing partial voltage curve and histogram data, as they complement each other and significantly enhance the accuracy and robustness of SOH estimation.

### 5.3.2. Overall accuracy improvement

The overall performance of three models, i.e. CNN-based SOH estimator using partial voltage curves, FNN-based SOH estimator using histogram data, and multi-modal fusion enabled SOH estimator, is compared across both the McMaster and Stanford datasets, as presented in Table 7 and Fig. 9.

For the McMaster dataset, the CNN-based SOH estimator using partial voltage curves achieves an RMSPE of 2.29 % over the whole testing dataset. As shown in Fig. 10 (a), most estimation points fall within a 5 % error band, with those exceeding 5 % error occurring primarily near the cell's end-of-life. This observation aligns with Fig. 2(e), which shows that cell resistance diverges significantly as cells age toward their end-of-life (70 % SOH). This resistance divergence worsens the mismatch between voltage curves and SOH, leading to poor estimation accuracy when relying solely on partial voltage curves.

An RMSPE of 27.3 % is recorded for the FNN-based SOH estimator using histogram data on the McMaster dataset, indicating that histogram data are insufficient for providing accurate SOH information in this

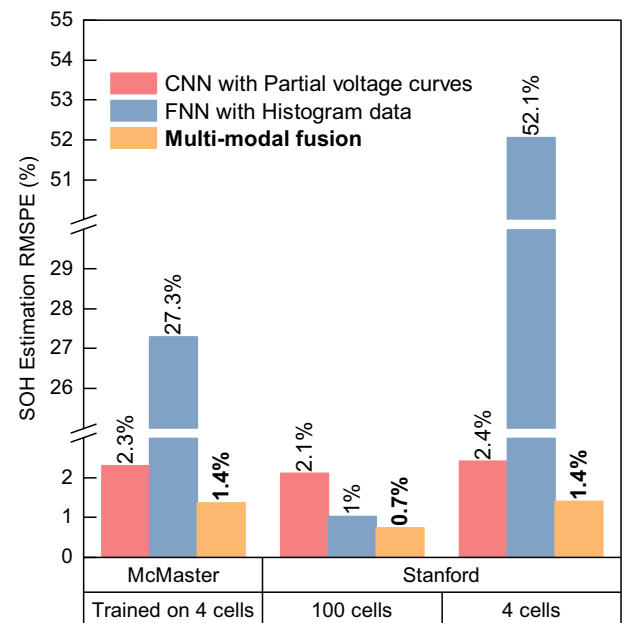


**Fig. 9.** SOH estimation accuracy results.

case. This limitation arises from the small size of the training dataset, which includes only 192 recorded aging cycles. Such a small data size is insufficient for model training due to a weak correlation between

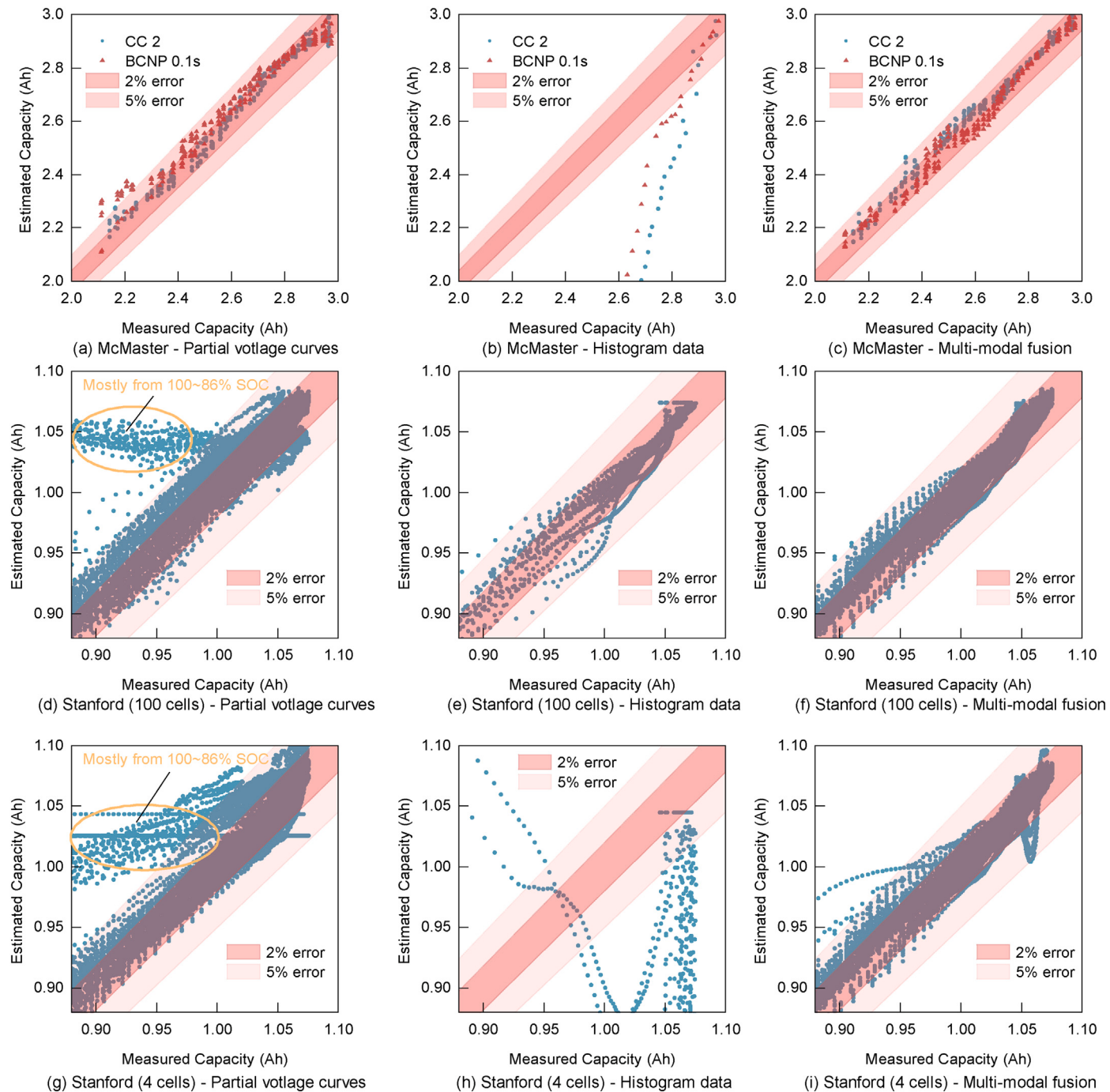


**Fig. 10.** Estimation results of three SOH estimators using both the McMaster and Stanford datasets. (a)–(c) show the estimated capacity by direct-captured HIs model, statistic-based HIs model, and multi-modal fusion model, respectively, versus the measured capacity using the McMaster dataset. The light-red and red areas are the bounds of  $\pm 5\%$  and  $\pm 2\%$  estimation errors. (d)–(f) show the estimated capacity by direct-captured HIs model, statistic-based HIs model, and multi-modal fusion model, respectively, versus the measured capacity on the Stanford dataset. (g)–(i) show the estimated capacity by direct-captured HIs model, statistic-based HIs model, and multi-modal fusion model trained from 4 selected cells, respectively, versus the measured capacity using the Stanford dataset. The abnormal estimation errors circled by yellow in (d) and (g) are mostly from the inputs located at the SOC range of 100 %–86 %. Note: The higher density in partial voltage and multi-modal fusion plots results from dividing charge curves into more partial data points.

histogram data and SOH, leading to poor estimation results. These findings underscore the inherent challenges in using partial voltage curves and histogram data individually for SOH estimation. To address these issues, we applied a multi-modal fusion model, which integrates both types of HIs. This model achieves an RMSPE of 1.36 %, representing an approximately 40 % improvement in estimation accuracy compared to the model using partial voltage curves alone.

For the Stanford dataset, the CNN-based SOH estimator using partial voltage curves achieves an RMSPE of 2.11 %. As presented in Fig. 10(d), significant estimation errors are observed when input partial curves are located in the SOC range of 100 %–86 %. This observation is due to similar voltage curves near a fully charged state, as shown in Fig. 8. FNN-based SOH estimator using histograms achieves an RMSPE of 1.03 %, highlighting the strong potential of histogram data when trained with

sufficient data size (73,743 recorded aging cycles). By combining both types of HIs together, our multi-modal fusion model achieves an RMSPE of 0.74 % and a MAPE of 0.50 %, which improves estimation accuracy by around 28 % compared to SOH estimator using only histogram-based HIs.

### 5.3.3. Less training data requirement

We designed a test case for the Stanford dataset where only 4 out of 100 cells were selected to train SOH estimators. This setup is similar to the McMaster dataset, representing the situations where training data are insufficient. Four representative cells (cell #2, 19, 37, 42) are selected to include as many diverse aging profiles as possible. In this case, the CNN-based SOH estimator utilizing partial voltage curves achieves an RMSPE of 2.41 %, which is slightly higher than the model trained with data from 100 cells (2.11 %). This indicates that partial voltage curves from a small dataset are already able to provide decent SOH information. In contrast, the histogram-based SOH estimator yields an RMSPE of 52.05 % when trained with insufficient data, performing significantly worse (52.05 % vs. 1.03 % RMSPE) compared to the case where 100 cells are used as the training set. This result again highlights the demand for massive training datasets when employing histogram-based HIs. By combining both information together, the proposed multi-modal fusion model achieves an RMSPE of 1.40 %, reducing error by approximately 42 % compared to the model that only uses partial voltage curves. As illustrated in Fig. 10(g) and (i), this improvement is mainly because the multi-modal fusion model successfully identifies SOH from data between 100 % and 86 % SOC, which partial voltage curves based HIs cannot achieve (a case study is presented in Fig. 8). In addition, the multi-modal fusion model trained with only four cells achieves an RMSPE that is approximately 34 % better than the partial voltage curves-based model trained with 100 cells (1.40 % versus 2.11 %).

To further evaluate the benefits of the multi-modal fusion model, we trained SOH estimators using subsets of the Stanford dataset comprising 4, 20, 30, 40, and 100 cells out of the total 100 cell training set. As shown in Fig. 11, the multi-modal fusion model consistently outperforms the model using only histogram data, regardless of the training data size. Notably, the multi-modal fusion model trained with 40 cells achieves an RMSPE of 1.01 %, outperforming the histogram-based model, which achieves an RMSPE of 1.03 %. This indicates that the multi-modal fusion model requires 60 % less training data to achieve comparable performance to the histogram-based model. These results underscore the effectiveness of the multi-modal fusion model in extracting SOH information, demonstrating its ability to reduce the size of the required training dataset. Furthermore, the multi-modal fusion model achieves reliable estimation accuracy with an RMSPE of 1.4 % when using only 4-cell training data. It enables our proposed model to perform effectively on a small dataset, demonstrating its superior robustness compared to other existing models.

### 5.4. Impact of transfer learning and fine-tuning

To evaluate the effectiveness of transfer learning in improving SOH estimation accuracy, we conducted a comparative analysis of three training configurations:

1. Baseline model trained from scratch (without transfer learning).
2. Model with locked pre-trained weights (transfer learning with frozen weights, as implemented in this study).
3. Model with unlocked pre-trained weights (transfer learning where weights are not frozen and remain trainable for fine-tuning).

This analysis was conducted using the Stanford dataset, where 100 cells were used as the training set. As summarized in Table 8, transfer learning significantly improves performance compared to training from scratch, reducing RMSPE from 0.89 % to 0.74 %. This suggests that leveraging pre-trained knowledge enhances feature extraction and

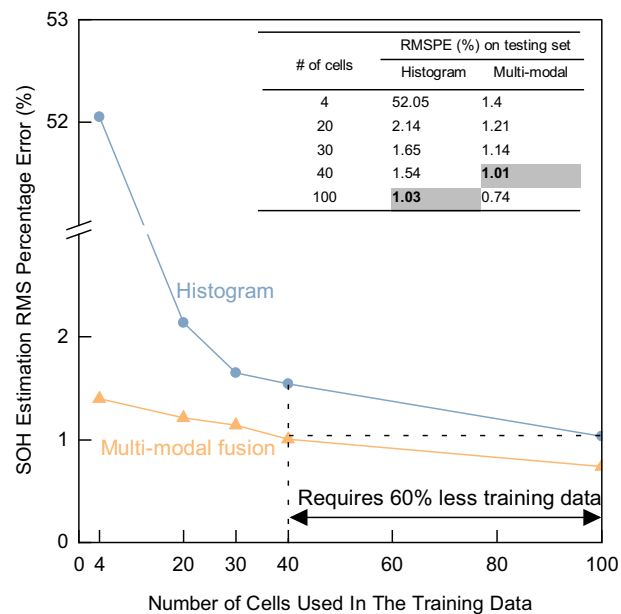


**Fig. 11.** SOH estimation results for the histogram-based and multi-modal fusion models on the Stanford dataset, trained with varying numbers of cells in the training data. Notably, the multi-modal fusion model requires 60 % less training data to achieve performance equivalent to that of the histogram-based model.

**Table 8**

Effect of transfer learning and fine-tuning on SOH estimation accuracy.

Model Configuration	RMSPE	MAPE
Baseline model trained from scratch (no transfer learning)	0.89 %	0.57 %
Model with locked pre-trained weights (transfer learning)	0.74 %	0.50 %
Model with unlocked pre-trained weights (transfer learning with fine tuning)	0.84 %	0.52 %

generalization. However, the fine-tuned model (0.83 %) performs worse than the locked pre-trained model (0.74 %), indicating that additional adaptation may distort previously learned representations or cause overfitting.

Fine-tuning allows the model to update pre-trained parameters for task-specific adaptation. However, in this study, it resulted in a slight decrease in accuracy. This can be attributed to various reasons: (1) Distortion of pre-trained feature representations. When all network parameters are unfrozen, the model may modify well-optimized features from pre-training, leading to suboptimal learning. (2) Overfitting. With all network parameters trainable, the model becomes significantly more complex and may become overly specialized in the training dataset. This can reduce its ability to generalize across different battery operating conditions.

These findings highlight the effectiveness of transfer learning for SOH estimation while emphasizing the importance of selecting an appropriate fine-tuning strategy. Based on our experimental results, freezing the pre-trained weights remains the optimal approach in this case, as it provides the best balance between accuracy and generalization.

### 5.5. Computational load analysis and onboard application feasibility

To demonstrate the real-world feasibility of our proposed model, we evaluated the model size and onboard execution time using the Stanford dataset, as shown in Table 9. The PC used for comparison is a 2021 Apple MacBook with an M1 chip, while the NVIDIA Jetson Nano, a compact,

**Table 9**  
Model size and execution time.

	Model size	Execution time* on PC	Execution time* on Jetson Nano
CNN with partial voltage curves	1.77 MB	0.15 ms	14.50 ms
FNN with histogram data	0.08 MB	0.0015 ms	0.1042 ms
Multi-modal fusion	1.97 MB	0.31 ms	15.63 ms

\* Execution time = total execution time/data points in the testing sets.

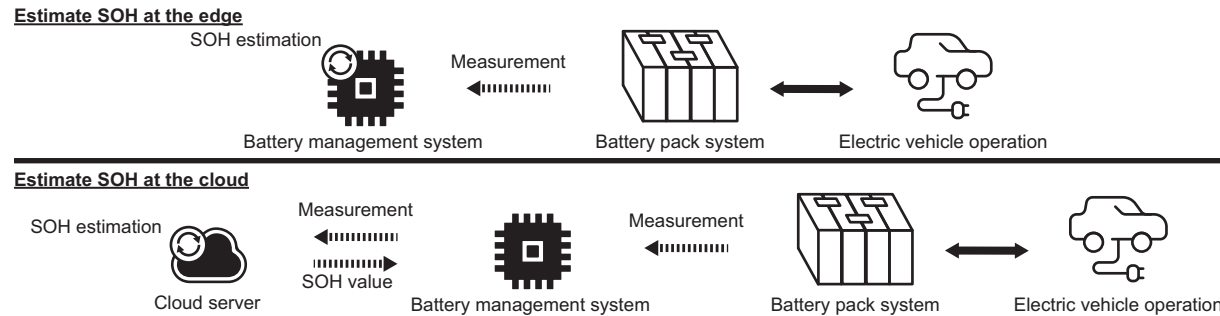


**Fig. 12.** Illustration of the SOH estimation model, which can be deployed at the edge and executed by the BMS or processed in the cloud server with the SOH value sent to the BMS.

energy-efficient edge AI computing board designed for embedded applications such as BMS, serves as a representative platform to assess the feasibility of onboard deployment in this study.

The FNN with a histogram data model is extremely light-weight (0.08 MB) and computationally efficient (0.1042 ms on Jetson Nano), making it ideal for low-power embedded applications. However, it is essential to note that the histogram-based model requires a significantly larger training dataset compared to other models to achieve comparable accuracy, as discussed in Fig. 11. The CNN with partial voltage curves model is moderately sized (1.77 MB), and its execution time is significantly higher (14.50 ms), indicating a higher computational cost. This is due to the complex structure of CNN layers and the high dimensionality of the input features. The multi-modal fusion model, despite its largest size (1.97 MB) and heavy computational load (15.63 ms), provides the most accurate results while not requiring extensive training datasets.

Although the multi-modal fusion model has the highest computational cost, it remains within the execution time constraints for real-time BMS applications, which typically require inference times below 100 ms per estimation. Additionally, since SOH estimation does not require continuous real-time execution but rather periodic updates (e.g. every charge-discharge cycle or at specific operational intervals), our model's processing time aligns with practical BMS constraints and achieves real-world feasibility.

If edge deployment is not feasible due to hardware limitations, an alternative approach is to use a cloud-based computing system, as illustrated in Fig. 12. In this case, the BMS collects battery measurements and transmits them to a cloud server for processing, with the SOH value sent back to the BMS after computation. This cloud-based architecture significantly reduces computational demands on the edge BMS, effectively addressing concerns related to intensive computation requirements in machine learning-based SOH estimation.

## 6. Conclusion

The data-driven model has been widely cited as the most promising approach for battery SOH estimation. However, existing HIs commonly have limitations regarding accuracy, practicality, and robustness. For instance, partial voltage and IC curves may lead to misleading SOH estimations, while histogram-based methods require extensive training data. To address these problems, we have introduced a novel multi-modal fusion model. The model introduces three key advantages:

1. **Reduced Training Data Requirements:** Unlike histogram-based SOH estimators, the proposed model requires a significantly smaller training dataset. This enhances its practicality, especially in real-world applications where massive and widely distributed datasets are typically unavailable.
2. **Robustness to SOC Window Variability:** The model is robust to variations in SOC window's range and location, avoiding the misleading SOH estimation results often encountered with partial voltage curve-based estimators.
3. **Improved Accuracy and Robustness:** By integrating different types of HIs, the multi-modal fusion model effectively mitigates their individual limitations, achieving superior estimation accuracy and robustness.

The models employed in this study were extensively optimized in terms of sizing and structure through extensive training on two representative experimental datasets. The proposed multi-modal fusion model demonstrated high effectiveness across both datasets, achieving a 1.36 % test error on a small dataset and a 0.74 % test error on a larger, more comprehensive dataset. Compared to other models, it further reduces SOH estimation errors by up to 42 % and requires 60 % less training data. Overall, this work demonstrates the feasibility and advantages of combining direct-captured and statistic-based HIs, underscoring the importance of detailed feature analysis in developing data-driven models for battery state estimation.

While this study demonstrates the effectiveness of a multi-modal fusion approach for battery SOH estimation, several areas remain open for future exploration and improvement. Below, we outline key directions that could further enhance the applicability and performance of data-driven SOH estimation models:

1. **Exploring Advanced Fusion Strategies:** The current fusion approach relies on a fully connected neural network to combine multi-modal features. Future research could investigate attention-based fusion mechanisms or graph-based neural networks to dynamically adjust the contribution of each HI type based on its reliability under different operating conditions.
2. **Enhancing Model Interpretability:** While our study focuses on improving SOH estimation accuracy through multi-modal fusion, future work can explore techniques to enhance model transparency. Methods like attention-based feature attribution could

- help explain how different HIs contribute to SOH predictions, making the model more interpretable and trustworthy for real-world applications.
- 3. Extending to Different Battery Chemistries and Applications:** Our model is validated on lithium-ion battery datasets, but future studies could assess its generalizability to other battery chemistries (e.g. solid-state, sodium-ion) and real-world electric vehicle (EV) applications. Investigating performance under varying operational conditions, such as high temperatures or ultra-fast charging scenarios, would further enhance its practical value.
- 4. Optimizing Transfer Learning through Fine-Tuning Strategies:** Our study demonstrates the benefits of transfer learning for SOH estimation; however, fine-tuning strategies require further investigation.
- 5. Balancing Accuracy and Deployment Efficiency:** Our study has demonstrated feasibility of real-time deployment on embedded BMS platforms. Future work will investigate model compression techniques to further reduce computational complexity, memory footprint, and energy consumption without significantly compromising SOH estimation accuracy.

By incorporating these future directions, we aim to inspire further advancements in SOH estimation research and encourage collaboration in enhancing battery health diagnostics.

#### CRediT authorship contribution statement

**Junran Chen:** Writing – review & editing, writing – original draft, visualization, validation, software, methodology, investigation, formal analysis, data curation, and conceptualization. **Phillip Kollmeyer:** Writing – review & editing, visualization, and supervision. **Ryan Ahmed:** Writing – review & editing and visualization. **Ali Emadi:** Writing – review & editing, supervision, project administration, and funding acquisition.

#### Declaration of competing interest

The authors declare that they have no known competing financial interests or personal relationships that could have appeared to influence the work reported in this paper.

#### Appendix A. Supplementary data

Supplementary data to this article can be found online at doi:10.1016/j.apenergy.2025.125923.

#### Data availability

I have shared the link to the data used in this work.

#### References

- Nishi Y. Lithium ion secondary batteries: past 10 years and the future. *J Power Sour* 2001;100(1):101–6. [https://doi.org/10.1016/S0378-7753\(01\)00887-4](https://doi.org/10.1016/S0378-7753(01)00887-4).
- Tomaszewska A, Chu Z, Feng X, O’Kane S, Liu X, Chen J, et al. Lithium-ion battery fast charging: a review. *eTransportation* 2019;1:100011. <https://doi.org/10.1016/j.etrans.2019.100011>.
- Pinson MB, Banzat MZ. Theory of SEI formation in rechargeable batteries: capacity fade, accelerated aging and lifetime prediction. *J Electrochem Soc* 2012;160(2):A243.
- Bond T, Gauthier R, Gasilov S, Dahn J. In-situ computed tomography of particle microcracking and electrode damage in cycled NMC622/graphite pouch cell batteries. *J Electrochem Soc* 2022;169(8):080531.
- Liu K, Wei Z, Zhang C, Shang Y, Teodorescu R, Han QL. Towards long lifetime battery: AI-based manufacturing and management. *IEEE/CAA J Autom Sin* 2022;9(7):1139–65. <https://doi.org/10.1109/JAS.2022.105599>.
- Li Y, Liu K, Foley AM, Zülke A, Berecibar M, Nanini-Maury E, et al. Data-driven health estimation and lifetime prediction of lithium-ion batteries: a review. *Renew Sustain Energy Rev* 2019;113:109254. <https://doi.org/10.1016/j.rser.2019.109254>.
- Martinez-Laserna E, Gandiaga I, Sarasketa-Zabala E, Badeda J, Stroe DI, Swierczynski M, et al. Battery second life: hype, hope or reality? A critical review of the state of the art. *Renew Sustain Energy Rev* 2018;93:701–18. <https://doi.org/10.1016/j.rser.2018.04.035>.
- Wei Z, Yang X, Li Y, He H, Li W, Sauer DU. Machine learning-based fast charging of lithium-ion battery by perceiving and regulating internal microscopic states. *Energy Storage Mater* 2023;56:62–75. <https://doi.org/10.1016/j.ensm.2022.12.034>.
- Ahmed R, El Sayed M, Arasaratnam I, Tjong J, Habibi S. Reduced-order electrochemical model parameters identification and state of charge estimation for healthy and aged li-ion batteries—Part II: aged battery model and state of charge estimation. *IEEE J Emerg Sel Top Power Electron* 2014;2(3):678–90. <https://doi.org/10.1109/jste.2014.2331062>.
- Tran M-K, Mathew M, Janhunen S, Panchal S, Raahemifar K, Fraser R, et al. A comprehensive equivalent circuit model for lithium-ion batteries, incorporating the effects of state of health, state of charge, and temperature on model parameters. *J Energy Storage* 2021;43:103252. <https://doi.org/10.1016/j.est.2021.103252>.
- Plett GL. Extended Kalman filtering for battery management systems of LiPB-based HEV battery packs: Part 3. State and parameter estimation. *J Power Sour* 2004;134(2):277–92. <https://doi.org/10.1016/j.jpowsour.2004.02.033>.
- Schwunk S, Armbruster N, Straub S, Kehl J, Vetter M. Particle filter for state of charge and state of health estimation for lithium–iron phosphate batteries. *J Power Sour* 2013;239:705–10. <https://doi.org/10.1016/j.jpowsour.2012.10.058>.
- Vidal C, Malyts P, Kollmeyer P, Enadi A. Machine learning applied to electrified vehicle battery state of charge and state of health estimation: state-of-the-art. *IEEE Access* 2020;8:52796–814. <https://doi.org/10.1109/access.2020.2980961>.
- Yang D, Wang Y, Pan R, Chen R, Chen Z. State-of-health estimation for the lithium-ion battery based on support vector regression. *Appl Energy* 2018;227:273–83. <https://doi.org/10.1016/j.apenergy.2017.08.096>.
- Zhang Y, Wik T, Bergström J, Pecht M, Zou C. A machine learning-based framework for online prediction of battery ageing trajectory and lifetime using histogram data. *J Power Sour* 2022;526:231110. <https://doi.org/10.1016/j.jpowsour.2022.231110>.
- Richardson RR, Birk CR, Osborne MA, Howey DA. Gaussian process regression for in situ capacity estimation of lithium-ion batteries. *IEEE Trans Ind Inf* 2019;15(1):127–38. <https://doi.org/10.1109/TII.2018.2794997>.
- Li W, Sengupta N, Dechent P, Howey D, Annaswamy A, Sauer DU. Online capacity estimation of lithium-ion batteries with deep long short-term memory networks. *J Power Sour* 2021;482:228863. <https://doi.org/10.1016/j.jpowsour.2020.228863>.
- Chen J, Manivanan M, Duque J, Kollmeyer P, Panchal S, Gross O, et al. A convolutional neural network for estimation of lithium-ion battery state-of-health during constant current operation. In: 2023 IEEE transportation electrification conference and expo (ITEC); 2023. p. 1–6. <https://doi.org/10.1109/ITEC55900.2023.10186914>.
- Guirguis J, Abdulmaksoud A, Ismail M, Kollmeyer PJ, Ahmed R. Transformer-based deep learning strategies for lithium-ion batteries sox estimation using regular and inverted embedding. *IEEE Access* 2024;12:167108–19. <https://doi.org/10.1109/ACCESS.2024.3495560>.
- Jiang N, Zhang J, Jiang W, Ren Y, Lin J, Khoo E, et al. Driving behavior-guided battery health monitoring for electric vehicles using extreme learning machine. *Appl Energy* 2024;364:123122. <https://doi.org/10.1016/j.apenergy.2024.123122>.
- Ramadass P, Haran B, Gomadam PM, White R, Popov BN. Development of first principles capacity fade model for Li-ion cells. *J Electrochem Soc* 2004;151(2):A196. <https://doi.org/10.1149/1.1634273>.
- Fan Y, Wang H, Zheng Y, Zhao J, Wu H, Wang K, et al. A novel state-of-health estimation method for fast charging lithium-ion batteries based on an adversarial encoder network. *J Energy Storage* 2023;63:107087. <https://doi.org/10.1016/j.est.2023.107087>.
- Acquareone M, Miretti F, Giuliaci TA, Duque J, Misul DA, Kollmeyer P. Regression based battery state of health estimation for multiple electric vehicle fast charging protocols. *J Power Sour* 2024;624:235601. <https://doi.org/10.1016/j.jpowsour.2024.235601>.
- Roman D, Saxena S, Robu V, Pecht M, Flynn D. Machine learning pipeline for battery state-of-health estimation. *Nat Mach Intell* 2021;3(5):447–56. <https://doi.org/10.1038/s42256-021-00312-3>.
- Zhu J, Wang Y, Huang Y, Bhushan Gopaluni R, Cao Y, Heere M, et al. Data-driven capacity estimation of commercial lithium-ion batteries from voltage relaxation. *Nat Commun* 2022;13(1):2261. <https://doi.org/10.1038/s41467-022-29837-w>.
- Dubarry M, Liaw BY. Identify capacity fading mechanism in a commercial lifepo4 cell. *J Power Sour* 2009;194(1):541–9. <https://doi.org/10.1016/j.jpowsour.2009.05.036>.
- Bian X, Wei Z, He J, Yan F, Liu L. A novel model-based voltage construction method for robust state-of-health estimation of lithium-ion batteries. *IEEE Trans Ind Electron* 2021;68(12):12173–84. <https://doi.org/10.1109/TIE.2020.3044779>.
- Hu X, Che Y, Lin X, Onori S. Battery health prediction using fusion-based feature selection and machine learning. *IEEE Trans Transp Electric* 2021;7(2):382–98. <https://doi.org/10.1109/TTE.2020.3017090>.
- She C, Li Y, Zou C, Wik T, Wang Z, Sun F. Offline and online blended machine learning for lithium-ion battery health state estimation. *IEEE Trans Transp Electric* 2022;8(2):1604–18. <https://doi.org/10.1109/TTE.2021.3129479>.
- Chemali E, Kollmeyer PJ, Preindl M, Fahmy Y, Emadi A. A convolutional neural network approach for estimation of Li-ion battery state of health from charge profiles. *Energies* 2022;15(3):1185.
- Lu Z, Fei Z, Wang B, Yang F. A feature fusion-based convolutional neural network for battery state-of-health estimation with mining of partial voltage curve. *Energy* 2024;288:129690. <https://doi.org/10.1016/j.energy.2023.129690>.

- [32] Greenbank S, Howey D. Automated feature extraction and selection for data-driven models of rapid battery capacity fade and end of life. *IEEE Trans Ind Inf* 2022;18(5):2965–73. <https://doi.org/10.1109/TII.2021.3106593>.
- [33] He Z, Shen X, Sun Y, Zhao S, Fan B, Pan C. State-of-health estimation based on real data of electric vehicles concerning user behavior. *J Energy Storage* 2021;41:102867. <https://doi.org/10.1016/j.est.2021.102867>. <https://www.sciencedirect.com/science/article/pii/S2352152X21005892>.
- [34] Wang Z, Yang F, Xu Q, Wang Y, Yan H, Xie M. Capacity estimation of lithium-ion batteries based on data aggregation and feature fusion via graph neural network. *Appl Energy* 2023;336:120808. <https://doi.org/10.1016/j.apenergy.2023.120808>.
- [35] Fei Z, Zhang Z, Tsui KL. Deep learning powered online battery health estimation considering multimescale aging dynamics and partial charging information. *IEEE Trans Transp Electric* 2024;10(1):42–54. <https://doi.org/10.1109/TTE.2023.3264438>.
- [36] You G-W, Park S, Oh D. Real-time state-of-health estimation for electric vehicle batteries: a data-driven approach. *Appl Energy* 2016;176:92–103. <https://doi.org/10.1016/j.apenergy.2016.05.051>.
- [37] Duque J, Kollmeyer PJ, Naguib M. Battery aging dataset for 15 minute fast charging of Samsung 30t cells; 2023. <https://doi.org/10.5683/SP3/UYPYDJ>.
- [38] Severson KA, Attia PM, Jin N, Perkins N, Jiang B, Yang Z, et al. Data-driven prediction of battery cycle life before capacity degradation. *Nat Energy* 2019;4(5):383–91. <https://doi.org/10.1038/s41560-019-0356-8>.
- [39] Sakoe H, Chiba S. Dynamic programming algorithm optimization for spoken word recognition. *IEEE Trans Acoust Speech Signal Process* 1978;26(1):43–9. <https://doi.org/10.1109/TASSP.1978.1163055>.
- [40] Chen J, Kollmeyer P, Chiang F, Emadi A. Lithium-ion battery state-of-health estimation via histogram data, principal component analysis, and machine learning. In: 2023 IEEE transportation electrification conference and expo (ITEC); 2023. p. 1–6. <https://doi.org/10.1109/ITEC55900.2023.10187012>.
- [41] Pearson K. Lii. On lines and planes of closest fit to systems of points in space. *Lond Edinb Dublin Philos Mag J Sci* 1901;2(11):559–72.
- [42] Pytorch: a machine learning library; 2016. <http://pytorch.org/>.